SOLUTION MINING RESEARCH INSTITUTE
679 Plank Road
Clifton Park, NY 12065, USA

Telephone: +1 518-579-6587
www.solutionmining.org

Technical Conference Paper

1965 – 2025

Mechanical Stability Following a Hydrogen Blowout in a Salt Cavern

Hippolyte Djizanne, Ineris
Parc technologique Alata, Verneuil-en-Halatte, France

SMRI Fall 2025 Technical Conference
29-30 September 2025
Wichita, Kansas, United States

Solution Mining Research Institute Fall 2025 Technical Conference

Wichita, Kansas, United States 29-30 September 2025

MECHANICAL STABILITY FOLLOWING A HYDROGEN BLOWOUT IN A SALT CAVERN

Hippolyte Djizanne

Ineris, Parc technologique Alata, Verneuil-en-Halatte, France

Abstract

Underground Hydrogen Storage (UHS) in salt caverns for energy purposes, will scale only if mechanical integrity under accidental scenarios is demonstrably robust. Among the critical hazards is a blowout: an uncontrolled release that drives rapid depressurization, severe gas cooling, and transient thermo-mechanical loads at the cavern wall.

This study quantifies the mechanical stability during and in the two weeks after a hydrogen blowout using coupled thermo-mechanical finite-element simulations for two real caverns (GA, GB), two discharge paths (casing vs. tubing), and two injection temperatures (30/45°C or *86/113°F*). The flow path controls discharge duration: 4 days for casing and 18-19 days for tubing; temperature acts mainly as a level shift. Near-wall cooling forms a thin area (approximately 5-10 m (*16-33 ft*)) with wall temperatures dropping to −27 to −15°C (*-17 to 5°F*), depending on the configuration.

The pressure-temperature trough produces rapid early convergence, with cumulative volume losses of approximately 2% (GA-casing, 30/45°C (*86/113°F*), 4 days), 2.7% (GB-casing, 45°C / *113°F*, 4 days), and 3.1% (GB-tubing, 45°C / *113°F*, 18 days). Following the blowout, additional losses of 0.46-0.96% accrue by +7/+14 days, while rates decay significantly.

Bérest effective stress criterion and the Factor of Safety maps confine tensile/dilatant conditions to a narrow wall-bounded annulus; the far field remains compressive ($FoS > 4$). Overall, the flow path is the primary driver of blowout persistence and cooling, whereas geometry/depth governs the magnitude; injection temperature is secondary.

The results delineate where damage is most likely (roof-proximal, first tens of meters (*30-100 ft*), provide quantitative bounds on capacity loss, and inform design and operating envelopes for safe hydrogen cavern storage.

Keywords: Blowout; hydrogen; salt caverns; thermo-mechanical coupling; convergence; Bérest effective stress; dilatancy; Factor of safety.

Introduction

A blowout (the uncontrolled release of gas from a storage well) is among the most severe incidents that can affect salt-cavern facilities. Although rare relative to the global fleet of caverns, documented events show that blowouts can last several days, expel the whole inventory, and trigger surface hazards ranging from flash and jet fires to unconfined vapor cloud explosions (UVCEs). For hydrogen, rapid depressurization also produces strong cooling that can load the cavern wall with transient thermo-mechanical stresses, raising concerns about dilatancy and near-wall damage. Recent syntheses have identified hydrogen blowouts as a priority topic for standardizing credible scenarios and safety distances around the wellhead (Buzogany et al., 2023, on SMRI Research Report RR2023-1). Against this backdrop, there is a need to translate the discharge physics (choked/subsonic flow, Joule-Thomson cooling, heat exchange) into mechanical indicators that matter for integrity: Bérest effective stress, Factor of safety (RD criterion), and convergence.

This study addresses that need by quantifying the mechanical stability during and after a hydrogen blowout in two real caverns (GA and GB). A coupled thermo-mechanical finite-element framework is used to simulate the full event for two discharge paths (casing vs. tubing) and two hydrogen injection temperatures (30°C, 45°C (*86/113 °F*)). Outputs include time histories of pressure and temperature, near-field temperature maps, stress/strain redistribution, dilatancy safety margins, and volume loss/convergence through the end of the blowout and into the first two weeks at atmospheric pressure (*1 atm = 14.7 psi*). *Although GA and GB are real caverns selected for the FrHyGe project, several assumptions are deliberately conservative and do not reflect their current operation: the caverns are taken to be 99% hydrogen at the maximum pressure at blowout onset, whereas in reality, both have been filled with brine since the end of their leaching in 2015. The simulations, therefore, represent worst-case behavior rather than site practice.*

Section 2 reviews prior works. Section 3 details the caverns, initial conditions and scenario matrix. Section 4 presents the results in three stages (pre-blowout baseline, discharge, and post-blowout response) to maintain a single causal chain from discharge to cooling, stresses, safety margins, and convergence. Section 5 discusses implications for design and operations, followed by discussion and conclusions.

1. Literature review

Documented blowouts from salt-cavern storage are rare relative to the global fleet; yet several well-reported cases anchor the present knowledge and motivate modeling. The SMRI incident database synthesizes leakage/overfilling/blowout events and shows that complete inventory loss can occur even where casualties are avoided. Moss Bluff (2004, natural gas) remains a key benchmark; other references include West Hackberry (1978, oil), Teutschental/Bad Lauchstädt (1984, town gas), and Fort Saskatchewan (2001, ethane) (Bérest & Brouard, 2003; incident compendia in Réveillère et al., 2017; case reports in Rittenhour & Heath, 2012; Halbgewachs et al., 2023, see Figure 1*a*; Brouard Consulting & RESPEC, 2013). Representative analyses emphasize multi-day duration and severe near-wall cooling as central integrity concerns (Djizanne et al. 2014).

The approach couples a cavern energy balance with a wellbore flow (Fanno model), predicting an initial choked stage (sonic at the wellhead) that transitions to subcritical flow near termination as pressure falls. This framework (developed and applied to gas-cavern blowouts) provides time histories of pressure, temperature, density, and velocity suitable for geomechanical boundary conditions (Bérest et al., 2013; Djizanne et al., 2014, Djizanne, 2014). Hydrogen-specific applications (EZ53, the selected cavern of the HyPSTER project) report a total duration of 3.65 hours, with 1.56 hours of choked flow, wellhead temperature minima near −60°C (*−76 °F*), and milder cavern-top minima near −20°C (*−4 °F*), consistent with Joule-Thomson cooling and significant transient heat uptake from the rock (Djizanne et al., 2022a,b). These studies also note model limits at very low flow and sensitivity to the chosen equation of state and friction correlations.

Finite-element studies resolve rock-gas heat exchange and the resulting stress/strain redistribution in the surrounding salt. A consistent picture emerges: rapid depressurization drives a thin, wall-bounded cooled area (meters to a few tens of meters; *30-100 ft*), a transient increase in tension at the wall, and a subsequent thermal recovery governed by conduction from the far field (Bérest & Brouard, 2003; Djizanne et al., 2014;

Djizanne et al., 2022a,b). Recent modeling frameworks incorporate viscoplastic creep (dislocation and pressure-solution mechanisms) and reproduce observed features of blowdown and post-event relaxation (Brouard et al., 2022; Brouard & Bérest, 2022).

Rock salt mechanical behaviour is elastoviscoplastic and highly sensitive to temperature. The time-dependent viscoplastic creep behavior is modeled using the Munson-Dawson multimechanism model (M-D model), as described by Munson (1997, 1998) and Munson et al. (1984, 1993). Two criteria are widely used to appraise damage propensity. The Bérest effective-stress criterion, $\sigma_{eff} = \sigma_{min} + P < T$, where *T* is salt tensile strength, flags zones where the least compressive principal stress plus cavern internal pressure becomes larger than the tensile strength; Coupled Thermo-Hydro-Mechanical (THM) studies typically confine such conditions to a narrow annulus adjacent to the wall. The RESPEC Dilation Criterion (RD Criterion from DeVries et al., (2005)) was used to evaluate the onset of salt dilation for this study; the derived Factor of Safety ($FoS > 1$ stable; $FoS \leq 1$ onset of dilatancy) helps to map a potential micro-fracturing area Djizanne et al., 2014; Djizanne et al., 2022a, Brouard et al., 2022). Recent work on salt damage mechanics provides constitutive tools to interpret such areas and their limited radial extent. The far field remains stable while the low-margin skin thickens as pressure approaches the atmospheric (*14.7 psi*) near-blowout end (e.g., recent SaltMech contributions such as Zaim et al., 2025; Habbani et al., 2025). Because blowouts impose a sudden drop from operating to near-atmospheric pressure (*14.7 psi*), deviatoric stresses at the wall rise, and creep closure accelerates, producing measurable volume loss over days to weeks. Predicted magnitudes scale with depth and inventory, with geometry and wellbore path modulating the rate history (Djizanne et al., 2014; Brouard et al., 2022).

Surface dispersion and safety distance should also be evaluated. Integrated assessments couple subsurface discharge to atmospheric dispersion/combustion to delineate safety zones. For hydrogen, early-time plumes can reach their maximum extent within minutes (Figure 1*b*), then contract as cavern pressure decays (e.g., dispersion envelopes in Djizanne et al., 2022a). Broader risk studies stress the need for standardized scenarios and metrics specific to hydrogen (Portarapillo & Di Benedetto, 2021; Buzogany et al., 2023).

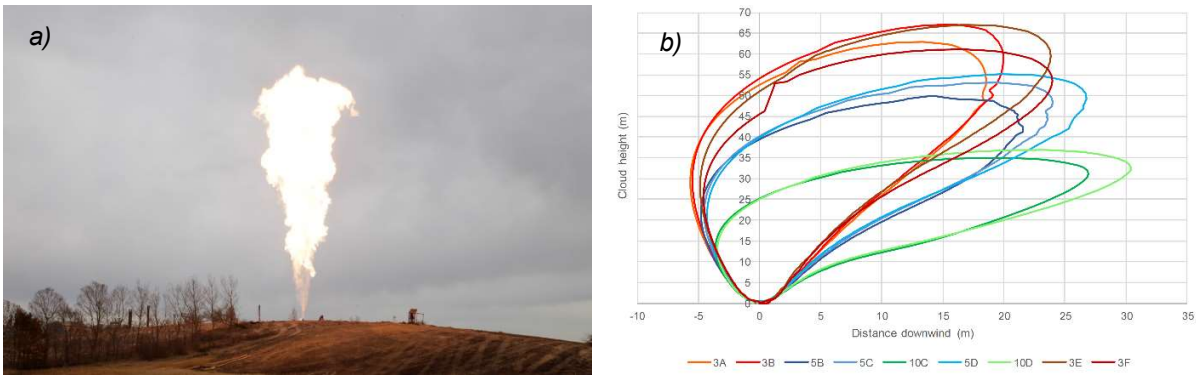

Figure 1. *a)* Natural Gas release through 7" casing during Prud'homme Cavern No. 1 blowout (Halbgewachs et al., 2023); *b)* Evolution of the hydrogen plume following a blowout in a salt cavern, one minute after the beginning of the blowout (contours: lower flammability limit of hydrogen, i.e., 40,000 ppm), from Djizanne et al., 2022.

Prior studies often analyze a single configuration or a generic cavern; model comparisons reveal sensitivity to thermodynamic data and end-of-event assumptions. A remaining need is a comparative, end-to-end evaluation that carries the chain from discharge (duration/regime) to near-field cooling, stresses/strains, dilatancy safety, and convergence; across multiple real caverns and completion paths under consistent assumptions. Zaim et al., (2025) underscore that such integrated appraisals are needed to bound the damage extent and to relate THM fields to operational stability criteria. The present study contributes to this line of research with two real caverns (GA/GB), two discharge geometries (casing vs. tubing), and two injection temperatures (30/45°C (*86/113°F*)), utilizing semi-analytical blowdown predictions coupled with THM simulations to quantify mechanical stability during and after a hydrogen blowout.

2. Case study presentation

2.1. Cavern and well completion (GA vs. GB)

Two caverns at the Manosque site (GA and GB) are considered as hydrogen storage cases for modeling purposes. Both are theoretically equipped with a $9⅝″$ casing and a $5½″$ tubing, with a uniform wall roughness $\varepsilon = 0.02\ mm$ (*0.0008 in*) (Table 1). Geometry differs mainly by depth and size:

- GA: well length to cavern roof 1,280 m (*4,199 ft*); total height 224 m (*735 ft*); max diameter 32 m (*107 ft*); volume 337,044 m^3 (*12 MMcf*); wall area 32,121 m^2 (*345,747 ft^2*).
- GB: well length 1,500 m (*4,921 ft*); total height 234 m (*768 ft*); max diameter 29.65 m (*97 ft*); volume 288,125 m^3 (*10 MMcf*); wall area 31,649 m^2 (*340,667 ft^2*).

These contrasts imply a larger gas inventory and heat-exchange area for GA, whereas GB is deeper and smaller, with greater hydrostatic head and slightly higher wellbore frictional losses. Note: GA and GB are real caverns, but the hydrogen configuration is a modeling assumption (*see Introduction scope note*). Table 1 summarizes GA and GB properties compared to a previous hydrogen blowout simulation of the EZ53 cavern of the HyPSTER project (Djizanne et al., 2022).

Table 1. Input parameters for hydrogen blowout modeling (EZ53 vs. GA, GB).

Property	EZ53	GA	GB
Gas (species)	Hydrogen	Hydrogen	Hydrogen
Gas initial pressure at cavern top	15 MPa (*2,205 psi*)	23 MPa (*3,292 psi*)	25 MPa (*3,611 psi*)
Gas initial temperature in the cavern	45°C (*113°F*)	45°C / 30°C (*113°F / 86°F*)	45°C / 30°C (*113°F / 86°F*)
Well length to cavern-top depth	920 m (*3,018 ft*)	1,280 m (*4,199 ft*)	1,500 m (*4,921 ft*)
Well diameter	*Tubing 7 5/8″*	*Casing 9 5/8″ / Tubing 5 1/2″*	*Casing 9 5/8″ / Tubing 5 1/2″*
Roughness (ε)	0.02 mm (*0.0008 in*)	0.02 mm (*0.0008 in*)	0.02 mm (*0.0008 in*)
Cavern total height	44 m (*144 ft*)	224 m (*735 ft*)	234 m (*768 ft*)
Cavern max diameter	20 m (*66 ft*)	32.47 m (*107 ft*)	29.65 m (*97 ft*)
Cavern volume	7,390 m³ (*260,975 ft^3; 0.26 MMcf*)	337,044 m³ (*11,9 10^6 ft^3; 12 MMcf*)	288,125 m³ (*10,2 10^6 ft^3; 10 MMcf*)
Cavern walls, overall surface	2,303 m² (*24,789 ft^2*)	32,121 m² (*345,748 ft^2*)	31,649 m² (*340,667 ft^2*)

3.2. Initial conditions

At the instant of blowout onset $t = 0+$, each cavern-well system is initialized to represent a conservative operating state just before venting:

- The cavern is assumed to be 99% hydrogen (1% residual brine) at the maximum pressure: 23 MPa for GA and 25 MPa for GB (Table 1).
- The hydrogen injection temperature in the cavern is 30°C or 45°C, depending on the case, and the cavern gas temperature is calculated with LOCAS software.
- Velocities and mass flow then follow from the computed pressure/temperature gradients along the selected discharge path (tubing or casing).

Figure 2 presents the initial geostatic pressure and geothermal temperature versus depth, with the top of the salt layer located between −912 m *(-2,992 ft*) and −855 m (*−2,810 ft*), and average cavern depths of −1,374 m (*−4,508 ft*) and −1,503 m (*−4,931 ft*). The geothermal profile implies far-field temperatures of approximately 45°C (*113°F*)at GA depth and 47°C (*117°F*) at GB depth; the shaded band in Figure 2

highlights this narrow range. The thermodynamic influence of the injected-gas temperature (density, speed of sound, and subsequent expansion cooling) is assessed from purely geometric effects.

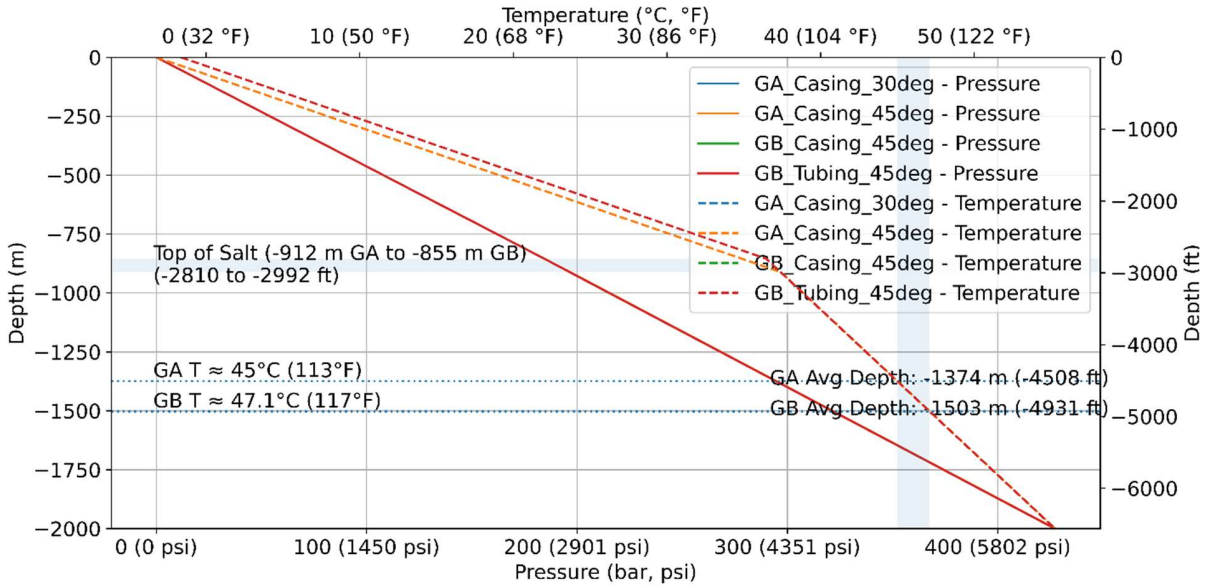

Figure 2. Depth profiles of geostatic pressure and geothermal temperature.

Rock salt mechanical behaviour is elastoviscoplastic and highly sensitive to temperature. The time-dependent viscoplastic creep behavior is modeled using the Munson-Dawson multimechanism model (M-D model), as described by Munson (1998). Generic salt parameters for the M-D model and the RD Criterion were assumed based on those used in Zaim et al., 2025.

2.3 Modelled scenarios

At $t = 0+$, the cavern-well system is assumed to be 99 % hydrogen (1% residual brine) and set to the maximum pressure (GA: 23 MPa (*3,292 psi*); GB: 25 MPa (*3,611 psi*), Table 1). The hydrogen injection temperature in the cavern is set to either 30°C (*86°F*) or 45°C (*113°F*). The wellhead is opened to atmospheric pressure (*14.7 psi*), and discharge occurs through either the tubing or the casing. All other inputs are fixed (gas: hydrogen; wall roughness ε = 0.02 mm (*0.0008 in*); completion diameters per Table 1).

The simulation matrix isolates three independent controls on blowout behavior:

- Site/geometry: GA (larger, shallower) vs. GB (smaller, deeper); governs inventory, heat-exchange area, and hydrostatic head.
- Discharge path: tubing (flow confined to the production string) vs casing (annular blowout); sets hydraulic section, frictional losses, and critical-flow conditions
- Injection temperature: 30°C (*86 °F*) or 45°C (*113 °F*); shifts initial density, sound speed, and the intensity of expansion/Joule-Thomson cooling.

This 2×2×2 design yields eight scenarios. Case IDs follow the format [cavern][path][Tinit] (e.g., GA_Tubing_30°C, GA_Casing_45°C, GB_Tubing_30°C, GB_Casing_45°C). These IDs are consistently used in the following figures and tables.

3. Results and interpretation

3.1. Before the blowout

3.1.1. Rock-mass behavior at baseline

The pre-blowout thermal state is close to geothermal (Figure 3). Temperatures range 42-50°C (*108-122 °F*) and increase with depth, with only a thin wall-bounded boundary layer (most visible near the roofs) marking heat exchange between the stored gas (nominal 45°C (*113 °F*)) and the salt. Beyond the first few meters, the formation follows the background gradient with negligible lateral anomalies. Differences between GA and GB at this stage are modest and reflect GB slightly greater depth and far-field temperature; completion type (casing vs tubing) has no discernible thermal imprint before the event.

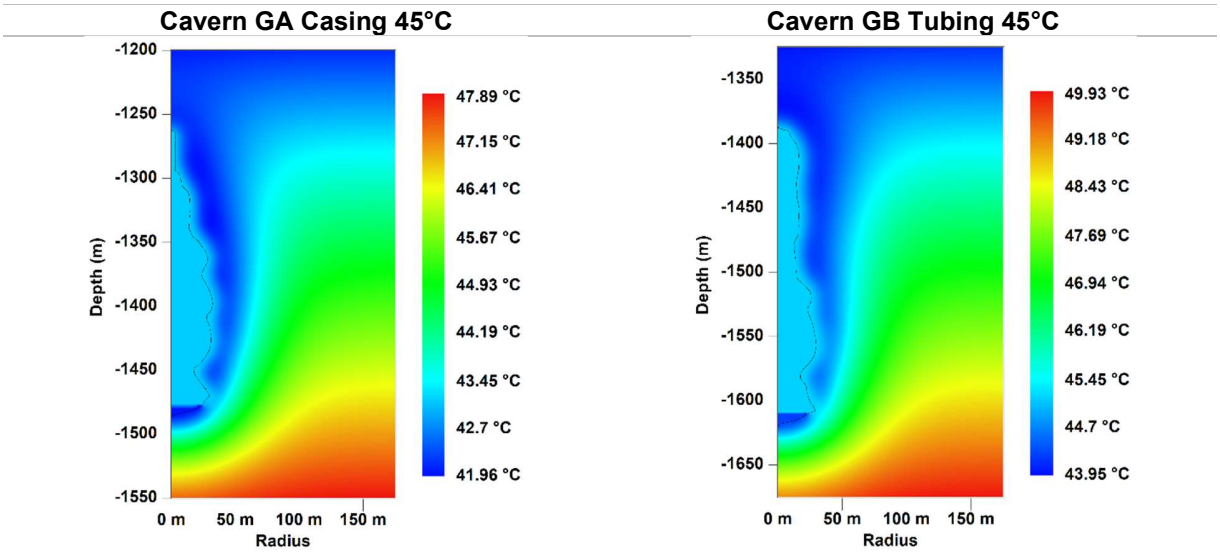

Figure 3. Temperature distribution before the blowout (GA 45°C; GB 45°C).

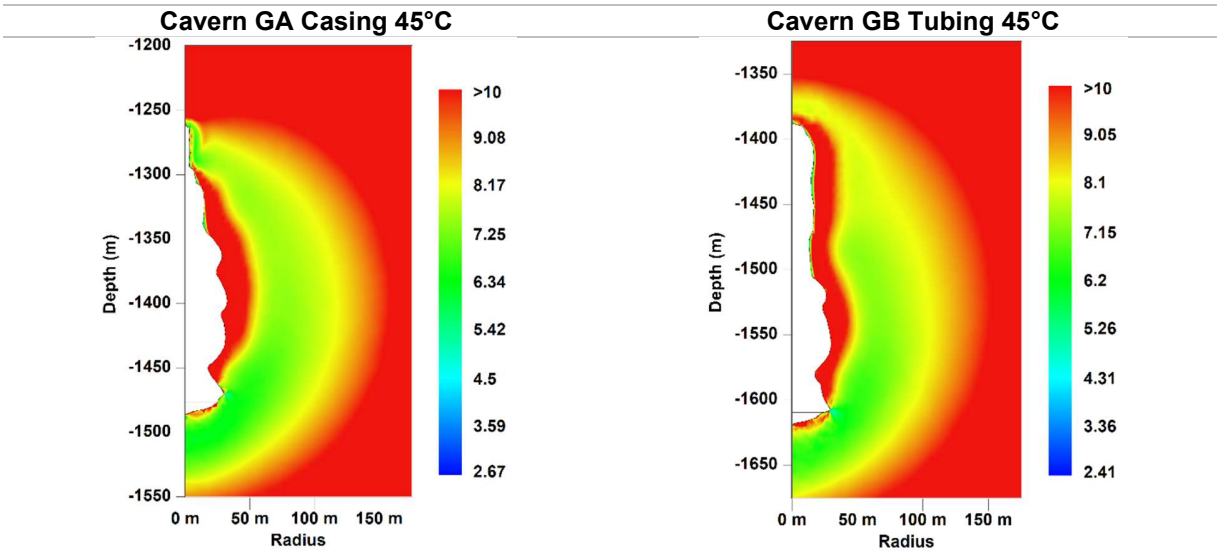

Figure 4. Factor of Safety (RD criterion) before the blowout; far field stable ($FoS \gg 1$).

Mechanically, the rock mass is in the stable domain (Figure 4). The Factor of safety relative to the RD dilatancy limit is ≫ 1 in the far field, with only a very thin annulus along the cavern wall showing reduced margins (FoS = 3-5) and minor local minima at the roof and floor where geometric stress concentrations are expected. No continuous dilatant zone (FoS ≤ 1) is present. This baseline establishes a stable reference state against which the blowout-induced cooling and pressure drop will be interpreted in §3.2.

3.1.2. Initial state at $t = 0+$

Figure 5 shows depth profiles of pressure, temperature, and specific volume immediately after opening the wellhead, for all eight GA/GB scenarios (casing vs. tubing; $T_{inj} = 30/45°C$ (*86/113°F*)). Depth is referenced from the wellhead (0 m at the surface, negative downward).

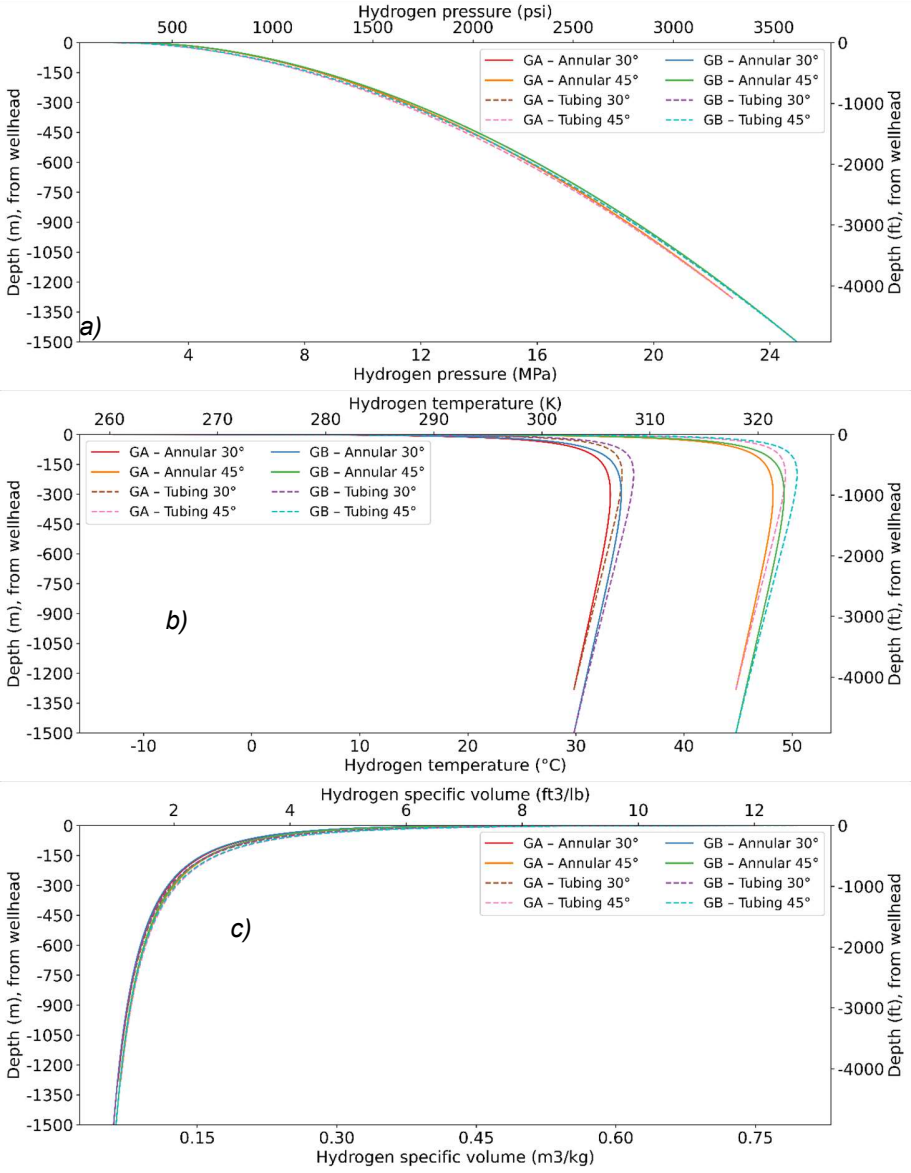

Figure 5. Distribution of pressure *a)*, temperature *b)*, and specific volume *c)* at the very beginning of the blowout, $t = 0+$.

In every case, pressure decreases monotonically upward from the cavern roof (about 23 MPa (GA, *3,292 psi*) and 25 MPa (GB, *3,611 psi*)) to atmospheric pressure (*14.7 psi*) at the wellhead (Figure 5*a*). At $t = 0+$, the casing and tubing curves are nearly the same because flow has not yet developed; GB lies slightly higher across the column due to its greater initial pressure and depth.

Temperature varies gently, shaped by real-gas isenthalpic behavior: where base-of-well velocities are modest, the Joule-Thomson sign for hydrogen at 30/45°C (*86/113°F*) produces upward warming as pressure drops (an effect an ideal-gas EOS would miss) while higher throughputs and wall exchange can flatten or invert local trends; depth-pooled medians are slightly higher in GB, and tubing cases tend to higher TTT, with the steepest gradient in GA-Tubing 45°C (Figure 5*b*).

Specific volume decreases with depth, with tubing being greater than annular at a given depth and 45°C (*113 °F*) being greater than 30°C (*86 °F*) as near-parallel shifts; medians are slightly higher in GA, and the steepest gradient (decreasing with depth) appears in GA-Tubing 45° (Figure 5*c*).

Overall, the initial hierarchy is established by site (depth and cavern-top pressure) and injection temperature, while the flow path becomes relevant only once significant discharge develops (§ 3.2). These $t = 0+$ profiles provide the baseline from which cooling, stresses, and convergence evolve.

3.2. During the blowout

During the blowout, the system transitions from a choked discharge to a subsonic regime, characterized by rapid cooling near the wall, stress redistribution at the cavern boundary, and time-dependent convergence. The analysis below links thermal transients to mechanical response (stresses, FoS) and to geometric change (convergence).

3.2.1. Blowout duration prediction

The blowout is computed using a fully coupled cavern-well model from $t = 0+$, with regime tagging based on the cavern-top conditions (§ 3.2): choked when $u_H \geq c_H$ and $P_H > 0.10\ MPa$; normal otherwise. Figure 6 gathers the time series of the main thermodynamic variables (pressures and temperatures at wellhead/cavern top, gas mass, mass flow, velocities, and rock-to-gas heat flux).

Total duration depends primarily on discharge geometry. Casing cases end after 4.0-4.4 days, whereas tubing cases persist for 17.6-19.5 days. Sensitivity to injection temperature (30 vs. 45°C or 86 vs. 113°F) is minor ($\lesssim$ 0.3 days at fixed geometry), and GB tends to be slightly shorter than GA for the same setup. Choked flow occupies roughly 40-50 % of the total in all configurations (e.g., GA-casing-30°C: 4.38 days = 2.08 days choked + 2.30 days normal; GA-tubing-45°C: 19.03 days = 8.09 days + 10.94 days; GB-casing-45°C: 3.95 days = 1.86 days + 2.09 days), see Table 2 and Table 3 for more key results of the blowout simulations.

Table 2. Blowout duration for each modeled scenario in days.

Cavern	Wellbore geometry	Injection temperature (°C / °F)	Blowout duration (days / h)	Fanno flow (days / h)	Normal flow (days / h)
GA	Casing	30 / 86	4.38 / 105.12	2.08 / 49.92	2.30 / 55.20
		45 / 113	4.27 / 102.48	2.04 / 48.96	2.23 / 53.52
	Tubing	30 / 86	19.47 / 467.28	8.26 / 198.24	11.21 / 269.04
		45 / 113	19.03 / 456.72	8.09 / 194.16	10.94 / 262.56
GB	Casing	30 / 86	4.04 / 96.96	1.90 / 45.60	0.86 / 20.64
		45 / 113	3.95 / 94.80	1.86 / 44.64	2.09 / 50.16
	Tubing	30 / 86	18.02 / 432.48	7.53 / 180.72	10.49 / 251.76
		45 / 113	17.61 / 422.64	7.37 / 176.88	10.24 / 245.76

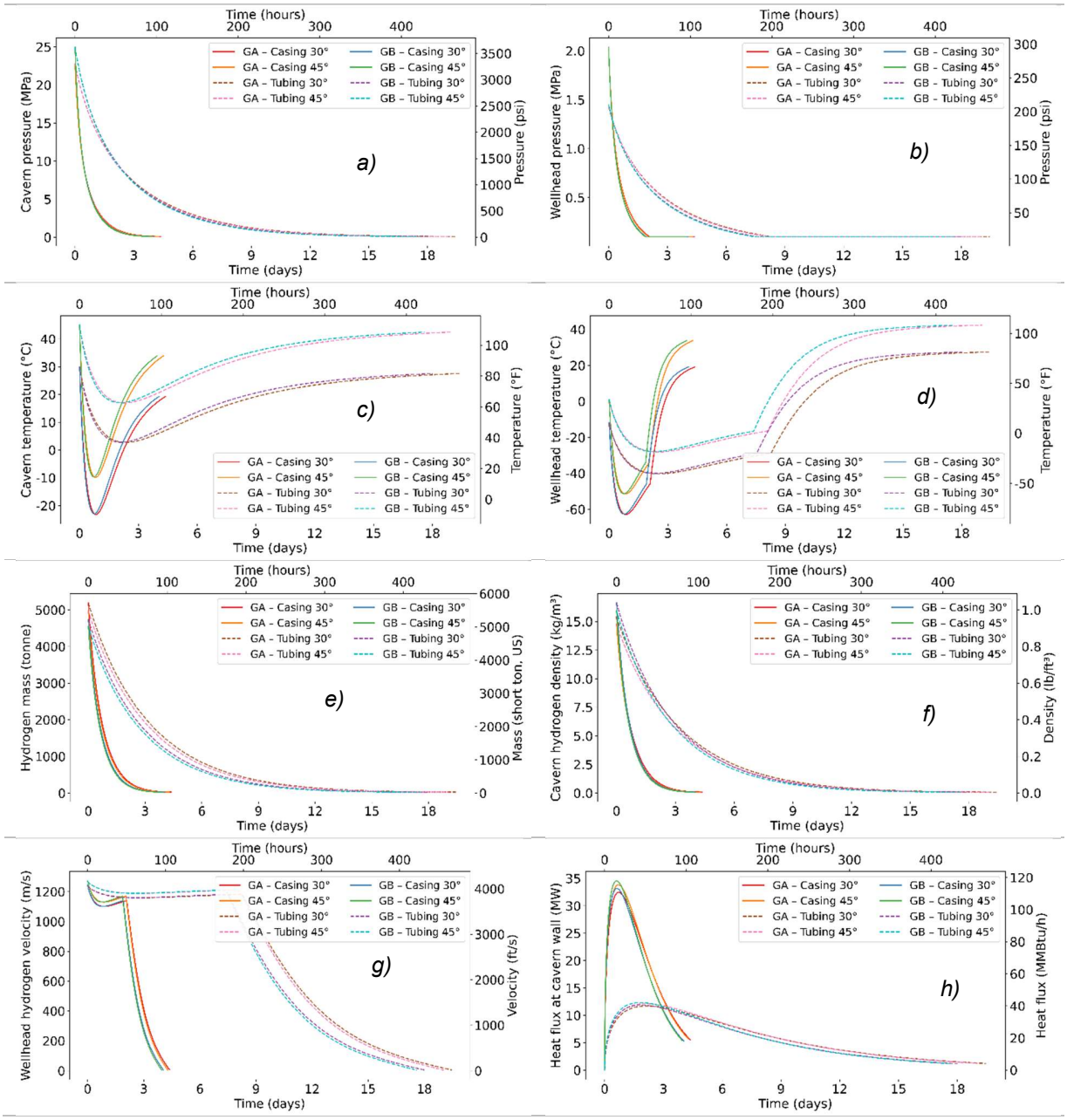

Figure 6. Time evolution of key thermodynamic variables during the GA and GB blowouts, two injection temperatures (30/45°C, (*86/113°F*)) and two discharge paths (tubing vs casing): *(a-b)* pressure at cavern top and at the wellhead; *(c-d)* temperature at cavern top and at the wellhead; *(e-f)* axial gas velocity at cavern top and at the wellhead; *(g-h)* mass-flow rate / total gas mass and rock-gas heat flux. Choked flow dominates early ($u \geq c$), with transition to normal flow as wellhead pressure approaches 0.10 MPa (*14.7 psi*).

Table 3. Summary of the results of blowout analysis on the EZ53 salt cavern.

Blowout Key Parameters	EZ53	GA - Casing 45°C	GB - Casing 45°C
Blowout duration	3.65 h *(0,15 days)*	102.48 h *(4.27 days)*	94.80 h *(3.95 days)*
Choked flow duration	1.56 h *(0.07 days)*	48.96 h *(2.04 days)*	44.64 h *(1.86 days)*
Normal flow duration	2.09 h *(0.08 days)*	53.52 h *(2.23 days)*	50.16 h *(2.09 days)*
Initial gas pressure	**15 MPa** *(2,205 psi)*	**23 MPa** *(3,292 psi)*	**25 MPa** *(3,611 psi)*
Ground-level pressure at the start of the blowout	1.4 MPa *(203.1 psi)*	2 MPa *(290 psi)*	2 MPa *(290 psi)*
Pressure at the cavern top at the end of the choked flow	1.08 MPa *(157 psi)*	1.1 MPa *(160 psi)*	1.2 MPa *(174 psi)*
Pressure at ground level at the end of the choked flow	0.10 MPa *(14.7 psi)*	0.10 MPa *(14.7 psi)*	0.10 MPa *(14.7 psi)*
Initial gas temperature	45°C *(113°F)*	45°C *(113°F)*	45°C *(113°F)*
Temperature at ground level at the start of the blowout	−2.6°C *(27.32°F)*	−0.02°C *(31.96°F)*	1.0°C *(33.80°F)*
Gas temperature at the cavern top at the end of the choked flow	−15°C *(5°F)*	11°C *(52°F)*	11°C *(52°F)*
Temperature at ground level at the end of the choked flow	−57°C *(−71°F)*	−34°C *(−29°F)*	−34°C *(−29°F)*
Lowest gas temperature in the cavern	−23°C *(−9°F)*	−10°C *(14°F)*	−10°C *(15°F)*
Lowest gas temperature at ground level	−63°C *(−81°F)*	−52°C *(−61°F)*	−51°C *(−60°F)*
Gas velocity at the cavern top at the start of the blowout	**147 m/s** *(482 ft/s)*	**151 m/s** *(495 ft/s)*	**142 m/s** *(466 ft/s)*
Gas velocity at ground level at the start of blowout	1,257 m/s *(4,124 ft/s)*	1,271 m/s *(4,169 ft/s)*	1,273 m/s *(4,177 ft/s)*
Gas velocity at the cavern top at the end of the choked flow	125 m/s *(410 ft/s)*	130 m/s *(427 ft/s)*	120 m/s *(394 ft/s)*
Gas velocity at ground level at the end of the choked flow	1,113 m/s *(3,651 ft/s)*	1,170 m/s *(3,839 ft/s)*	1,170 m/s *(3,839 ft/s)*
Cavern volume	**7,390 m^3** *(0.261 MMcf)*	**337,044 m^3** *(11.903 MMcf)*	**288,125 m^3** *(10.175 MMcf)*
Initial gas mass	77 t *(85 short tons)*	4,973 t *(5,482 short tons)*	4,548 t *(5,013 short tons)*
Maximum heat flux from the cavern wall	11 MW *(37.5 MMBtu/h)*	34 MW *(116.0 MMBtu/h)*	35 MW *(119.4 MMBtu/h)*
Mass flow at the start of the blowout	**36 kg/s** *(80 lb/s)*	**90 kg/s** *(199 lb/s)*	**92 kg/s** *(202 lb/s)*
Wellbore diameter	**7 5/8″**	**9 5/8″**	**9 5/8″**

P_H, the wellhead pressure and P_0, the cavern pressure decay monotonically from their initial values toward the cutoff threshold $P_H = 0.10\ MPa$ (*14.7 psi*) that defines the end of the event. Early-time near-sonic discharge at the wellhead is evident ($u_H = 1.2 - 1.3\ km\ s^{-1}$ (*3,937-4,265 ft/s*), while cavern-top velocities are an order of magnitude lower ($u_0 = 120 - 130\ m\ s^{-1}$) or (*394 - 427 ft/s*), reflecting acceleration in the conduit.

The wellhead gas cools sharply, reaching sub-zero minima (as low as −40 to -60°C (*-40 to -76°F*) depending on scenario), whereas the cavern-top minimum is much milder (typically −3 to -20°C (*27 to −4 °F*)). This pattern is consistent with expansion/Joule-Thomson cooling concentrated at the restriction and partially offset by rock-to-gas heat transfer.

The gas mass decreases rapidly from 5,000 tons (*5,512 short tons*) at first and then asymptotically, mirroring the mass-flow peak followed by a long tail. Peak thermal power drawn from the cavern wall is ample (order 20-25 MW (*68-85 MMBtu/h*)), documenting an intense transient enthalpy flux from the rock that limits the minimum temperatures in the cavern. Geometry controls duration, while injection temperature primarily shifts absolute temperature levels without altering the regime sequence. The sustained choked interval across all cases indicates that the critical pressure ratio at the wellhead is maintained until the reservoir is nearly depleted; the subsequent normal-flow tail governs the final approach to atmospheric pressure (*14.7 psi*). These thermodynamic transients provide the context for the near-field cooling (§ 3.2.2), convergence (§ 3.2.3), and stability margins (§ 3.2.4) discussed next.

3.2.2. Near-field temperature evolution during the blowout

This subsection tracks how the rock-gas temperature field evolves from onset to the end of the blowout for two representative paths at the same nominal injection temperature (45°C (*113°F*): GA-casing and GB-tubing. At $t = 0+$, both caverns are near their pre-event thermal state (42-50°C (*107-122 °F*) with only a thin wall-bounded boundary layer; the far field follows the geothermal gradient.

By the end of the blowout (Figure 7), a cooled annulus surrounds each cavern while the far field remains close to geothermal. In GA-casing, cooling spans almost the full height of the wall and penetrates (10 m (*33 ft*)) into the salt; near-wall temperatures are 10°C (*50°F*), i.e., $a > 30°C$ (*86°F*) drop from the initial state. In GB-tubing, the pattern is similar but more localized: the cold skin is thinner, radial gradients are steeper, and the minimum near-wall temperature is approximately 28°C (*82°F*), indicating a smaller net heat extraction.

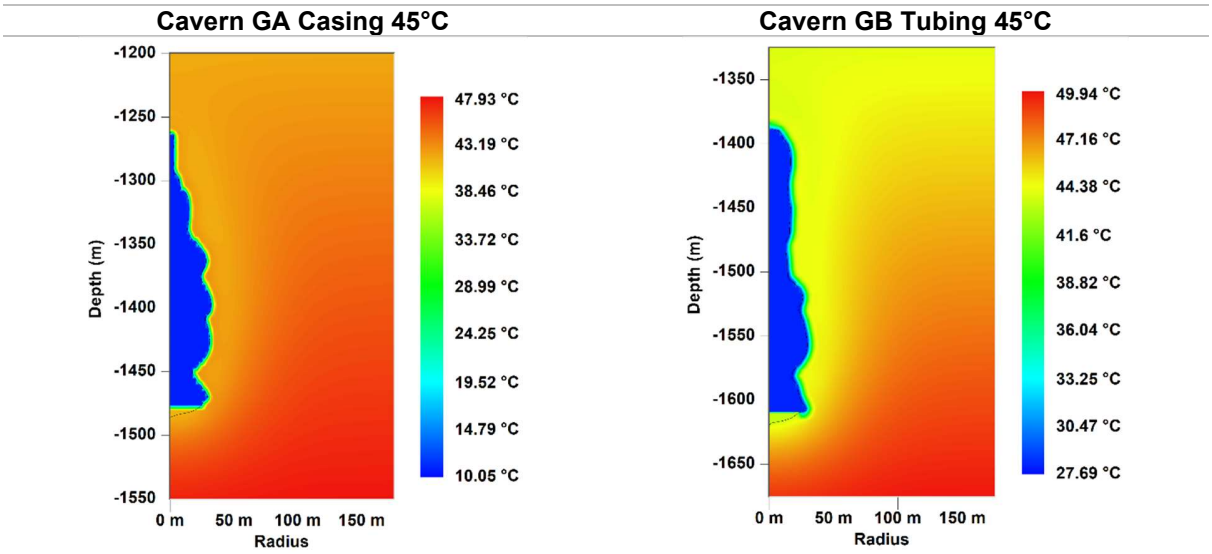

Figure 7. Temperature around the cavern at the end of the blowout (GA casing 45°C; GB tubing 45°C).

Roof and mid-depth profiles (Figure 8) indicate that the temperature jumps from its near-wall minimum to near-geothermal values within approximately 5-10 m (*16-33 ft*); beyond approximately 50 m (*164 ft*), the curves are nearly indistinguishable. GA exhibits a broader depression than GB at both levels, consistent with the casing path distributing exchange along the wall, whereas tubing confines it.

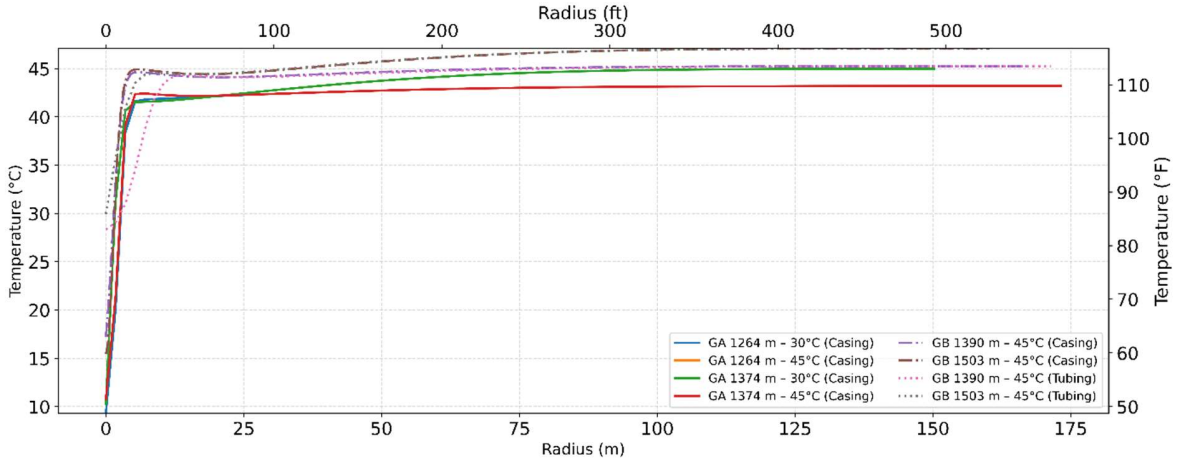

Figure 8. Radial temperature profiles at the cavern roof and mid-depth.

The selected cavern wall-node histories in the upper cavern (Figure 9) reach their coldest phase within 0.4-0.8 days, with minima between −27 and −15°C (*−17 and 5 °F*) depending on configuration, followed by gradual reheating driven by conduction from the rock and internal mixing. Despite this recovery, the wall remains sub-geothermal at the end of the event (more so for GA), matching the larger cooled volume inferred from Figures. 8-9.

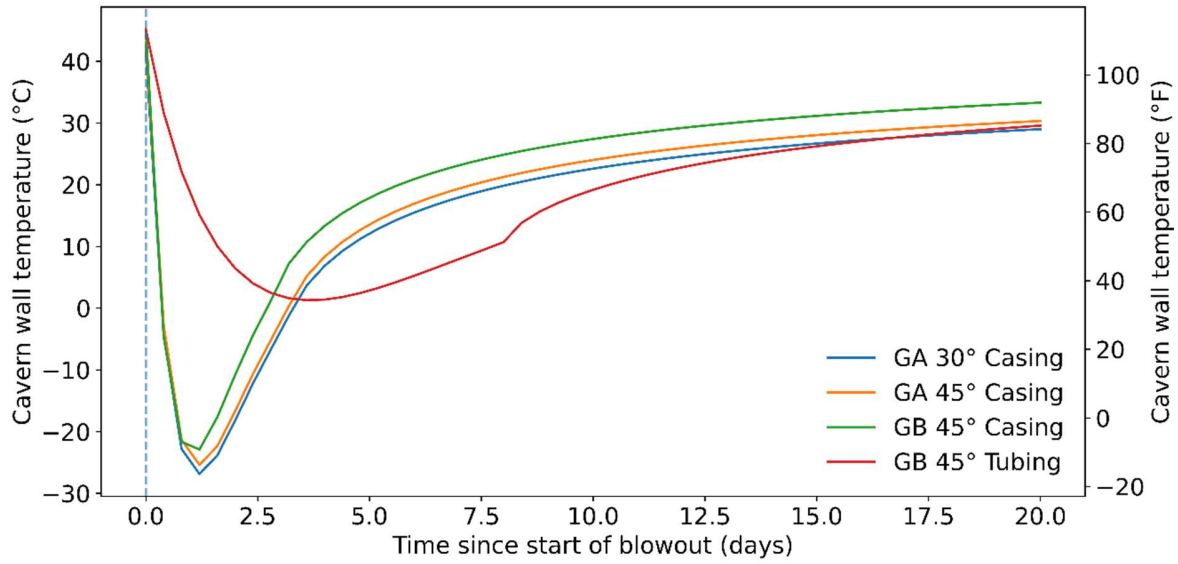

Figure 9. Temperature vs. time at a cavern wall node in the upper cavern.

The wall-adjacent cooling introduces tensile thermal components in the stress, preconditioning the near-wall zone for reduced RD dilatancy margins discussed in §§ 3.2.4-3.2.5.

3.2.3. Cavern volume loss and cavern convergence

Rapid depressurization during the blowout increases deviatoric stress at the wall and accelerates viscoplastic creep, resulting in net cavity convergence. Convergence is measured as fractional volume loss.

$$C(t) = -(V_0 - V(t))/V_0 \times 100\%$$

With V_0 the initial cavern volume (GA 337,044 m³ (*12 MMcf*); GB 288,125 m³ (*10 MMcf*) and $C(0) = 0\%$.

Cumulative loss is presented in Figure 10. Over their respective windows, the cavern volume losses at the end of the blowout are:

- GA: Casing 30°C: 2.0 % at 4.38 days
- GA: Casing 45°C: 2.0 % at 4.27 days
- GB: Casing 45°C: 2.7 % at 3.95 days
- GB: Tubing 45°C: 3.1 % at 17.61 days

GA at 30°C (*86 °F*) and 45°C (*113 °F*) are nearly indistinguishable, indicating limited sensitivity to the initial temperature over 4 days. GB shows larger losses; the tubing case converges longer and ends higher due to its extended duration.

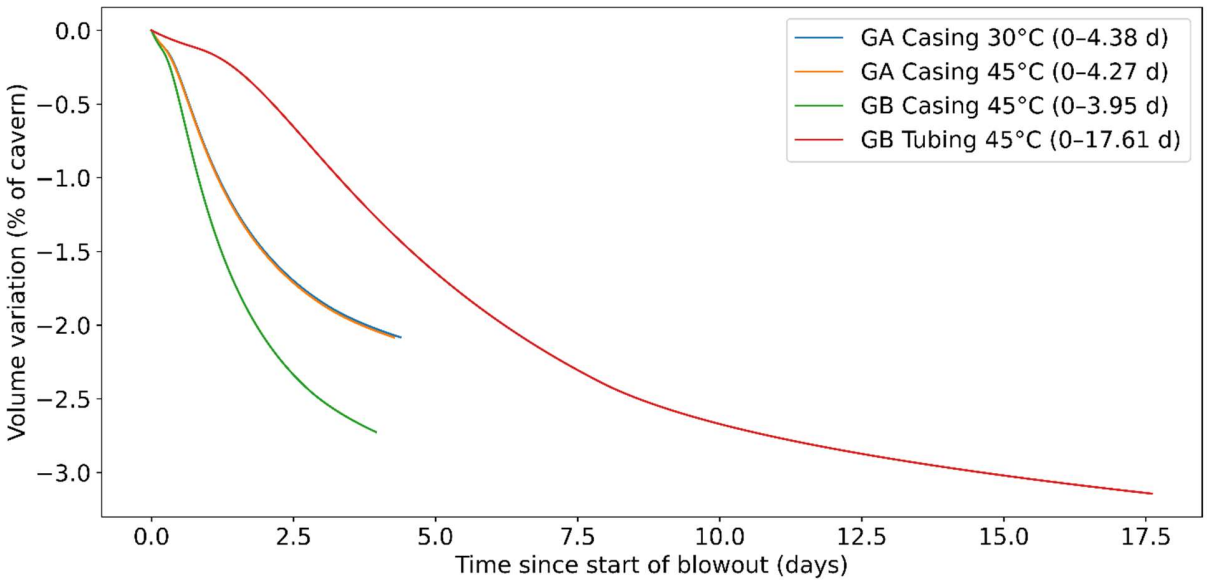

Figure 10. Cumulative cavern convergence during the blowout (volume loss, % of cavern).

For the instantaneous speed (Figure 11), the convergence rate is computed as:

$$v(t) = -dC/dt \times 365 \text{ (\% of cavern per year)},$$

With the sign chosen positive denotes loss. All series display a sharp early peak within the first day, then a monotonic decay:

- GB Casing 45°C: peak 550-600 % yr⁻¹
- GA Casing (30/45°C (*86/113°F*)): peak 250-350 % yr⁻¹
- GB Tubing 45°C: lower peak 120-160 % yr⁻¹ but persists the longest, declining to 25-30 % yr⁻¹ by day 18

Small wiggles in $v(t)$ reflect the differentiation of discretely sampled data, rather than physical oscillations. To conclude this section, it can be noted that convergence is fast but front-loaded: most occurs early, coincident with the temperature trough mapped in § 3.2.2; flow path is the primary control, casing produces a sharper, higher peak, tubing a milder but more prolonged response; depth/geometry (GB vs GA) sets

overall magnitude. These trends anticipate the wall-stress excursions and stability margins discussed next (§3.2.4-§3.2.5).

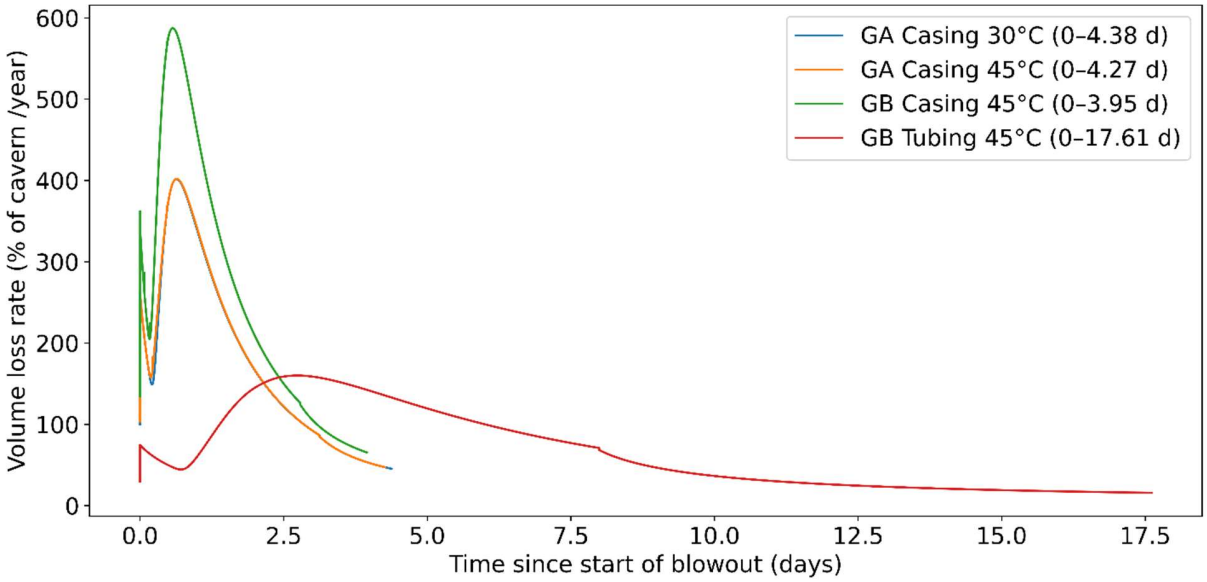

Figure 11. Instantaneous convergence rate during the blowout (% of cavern per year).

3.2.4. Stresses and strains at the cavern wall

At the cavern wall, the radial (normal) stress equals the opposite of the cavern internal pressure, $\sigma_{rr} = -P_0$ (compression negative). Tensile propensity is evaluated using the Bérest effective stress, $\sigma_{eff} = \sigma_{min} + P_0$, where σ_{min} is the least compressive principal stress at the cavern wall and P_c is the cavern internal pressure. $\sigma_{eff} > 0$ indicates tension (fracture-prone), and $\sigma_{eff} \leq 0$ indicates compression.

Both GA-casing 45°C and GB-tubing 45°C show a thin, wall-bounded annulus of near-zero to slightly tensile σ_{eff}, strongest near the roof and locally at geometric re-entrants. Within a few meters, the field turns compressive ($\sigma_{eff} = -1\ to\ -6\ MPa$, or *−145 to −870 psi*) and the far field remains safely compressive (see Figure 12).

The GA-casing case presents a more continuous, low-margin band along the wall height, whereas the GB-tubing exhibits a narrower, more localized band with steeper radial recovery, consistent with the more localized cooling of the tubing configuration (§ 3.2.2).

Figure 13 plots the maximum principal strain ε_{max} (tension is positive) as a function of radius from the cavern wall, evaluated at the roof and at mid-depth for GA and GB, with initial gas temperatures of 30 °C (*86 °F*) and 45 °C (*113 °F*), and casing or tubing discharge paths.

The strain response is likewise strongly localized. Peak tensile strains at the wall are about 1.0-1.3 % for GA-casing (30/45°C (*86/113°F*)), up to 3-3.5 % for GB-casing 45°C, and 1 % for GB-tubing 45°C. Strain decays rapidly with radius, typically <0.2 % by 20-30 m (*66-98 ft*), <0.05 % by 75-100 m (*246-328 ft*), and near zero beyond 150 m (*492 ft*). Roof profiles are slightly higher than mid-depth, aligning with the stronger roof-proximal cooling. For a given cavern/path, initializations at 30°C (86°F) yield modestly larger peaks than those at 45°C (*113 °F*). Overall, a practical affected thickness is 20-30 m (*66-98 ft*, where $\varepsilon_{max} = 0.1$). These stress-strain signatures anticipate the RD dilatancy margins mapped next (§ 3.2.5): a thin near-wall area of reduced stability with a compressive far field.

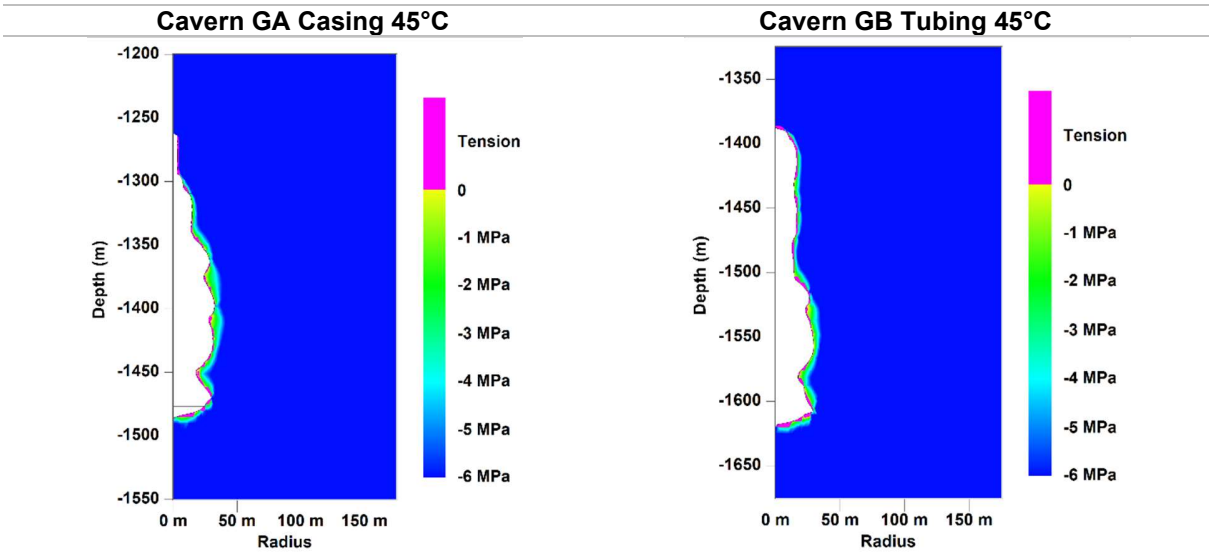

Figure 12. Bérest effective stress $\sigma_{eff} = \sigma_{min} + P_H$ at the end of the blowout (positive = tension). Both caverns show a thin near-wall band of near-zero/slightly tensile values (strongest near the roof) while the far field remains compressive.

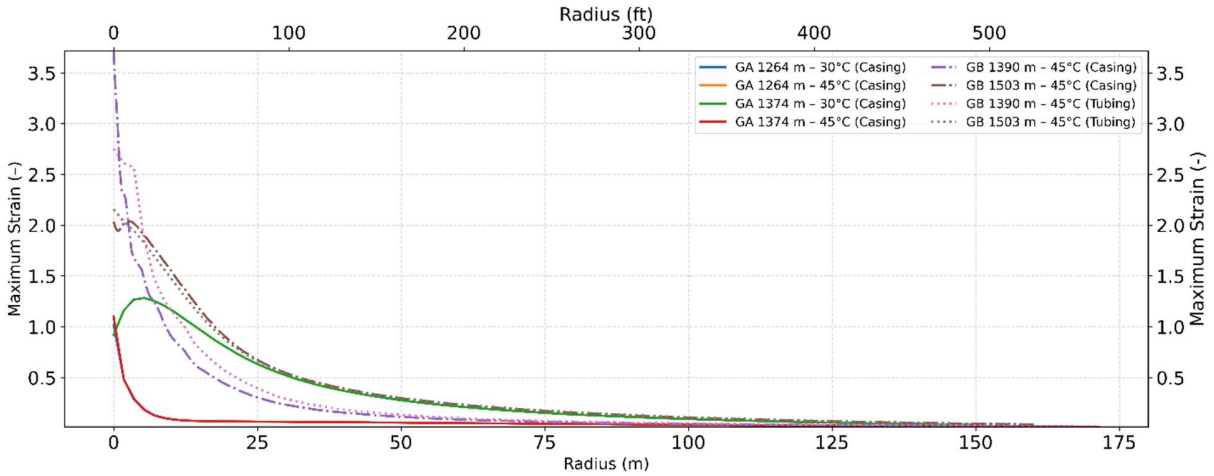

Figure 13. Maximum principal strain ε_{max} versus radius at the cavern roof and mid-depth for GA and GB (30/45°C (*86/113 °F*); casing/tubing), evaluated at the end of the blowout. Tension positive; strain localizes within the first 20-30 m (*66-98 ft*) and decays to near zero by 100-150 m (*328 ft-492 ft)*.

3.2.5. Factor of safety against dilatancy (RD criterion)

At baseline (Figure 4), the rock mass is stable with $FoS \gg 1$ and no continuous dilatant zone. By the end of the blowout (Figure 14), the combined effects of depressurization and near-wall cooling lower mean stress and raise deviatoric stress at the boundary, producing a continuous, wall-bounded area with $FoS \leq 1$ (Magenta color). This area is thin (only a few to approximately 10 m (*33 ft*))and is surrounded by a broader ring with $FoS = 1.5 - 3$. The far field remains stable ($FoS > 4$).

Comparing configurations, GA-casing-45°C develops a thicker and more vertically continuous low-FoS band, particularly near the roof, consistent with its broader/colder thermal boundary layer and faster early depressurization. GB-tubing-45°C shows a narrower, more localized anomaly with steeper radial recovery,

mirroring its more confined cooling pattern (§ 3.2.2). These maps align with the effective-stress and strain results (§ 3.2.4), which likewise confine reduced stability margins to a thin near-wall skin, while the surrounding formation remains stable.

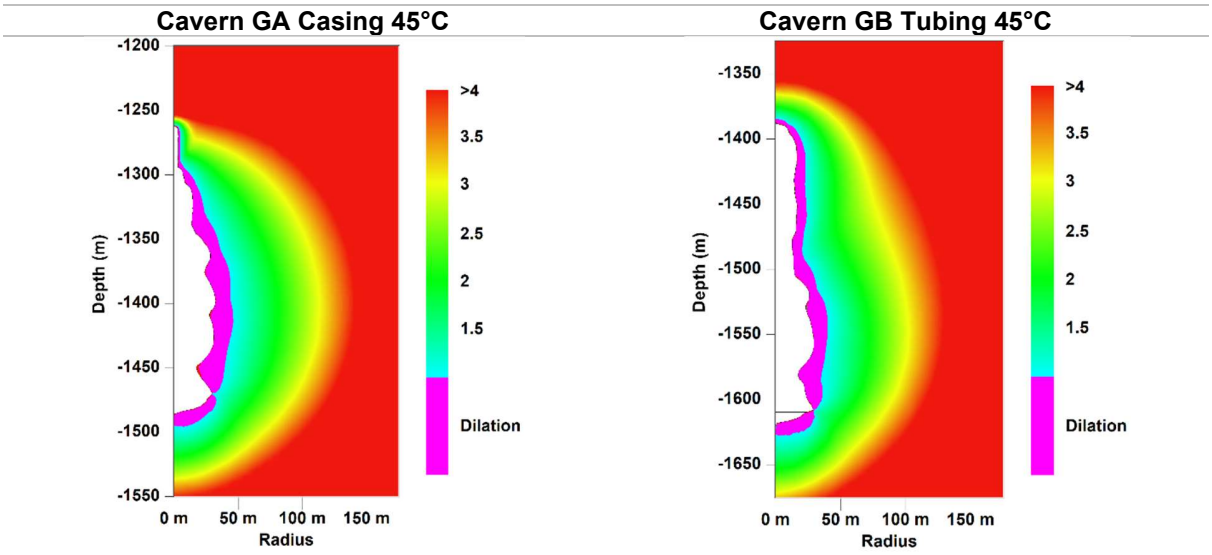

Figure 14. Factor of Safety (FoS, RD criterion) at the end of the blowout (GA casing 45°C; GB tubing 45°C). Magenta color indicates $FoS \leq 1$ (dilatancy); far field $FoS > 4$.

3.3. After the blowout

This section documents the short-term mechanical response seven and fourteen days after the blowout, with cavern pressure held at atmospheric (*14.7 psi*). These two milestones capture the transition from the immediate transient to a slower, creep-controlled regime. The depth and extent of wall damage are known to increase with blowout duration (Brouard Consulting & RESPEC, 2013); duration and associated safety distances depend on cavern volume/inventory, pressure, depth, and flow path, as shown earlier. Three indicators are examined: convergence, Factor of safety (FoS), and displacements.

3.3.1. Cavern convergence

Once venting stops, convergence continues by viscoplastic creep but decelerates quickly. For the GA-casing 45°C case, the additional loss relative to the end-of-event is approximately 0.46-0.65% of the cavern volume by day 7 (1.6-1.8 × 10^3 m^3), with instantaneous rates still elevated (15-21% yr^{-1}, i.e., 140-160 m^3 per day). By day 14, the cumulative increment reaches 0.69-0.96% (2.3-2.8 × 10^3 m^3) and rates fall to 10-14% yr^{-1} (90-110 m^3 d^{-1}). Hence, most post-blowout closures occur in the first week, followed by a transition to a moderate creep regime.

3.3.2. Factor of safety

Figure 15 maps the RD-based FoS for GA-casing-45°C at +7 and +14 days after the blowout. A thin, wall-bounded dilatant skin ($FoS \leq 1$, Magenta color) persists at both times, encircled by a buffer with a FoS of approximately 1.5-3. The far field remains stable ($FoS > 4$). Between +7 and +14 days after the blowout, contours shift to higher FoS, indicating stabilization without outward propagation of the dilatant area.

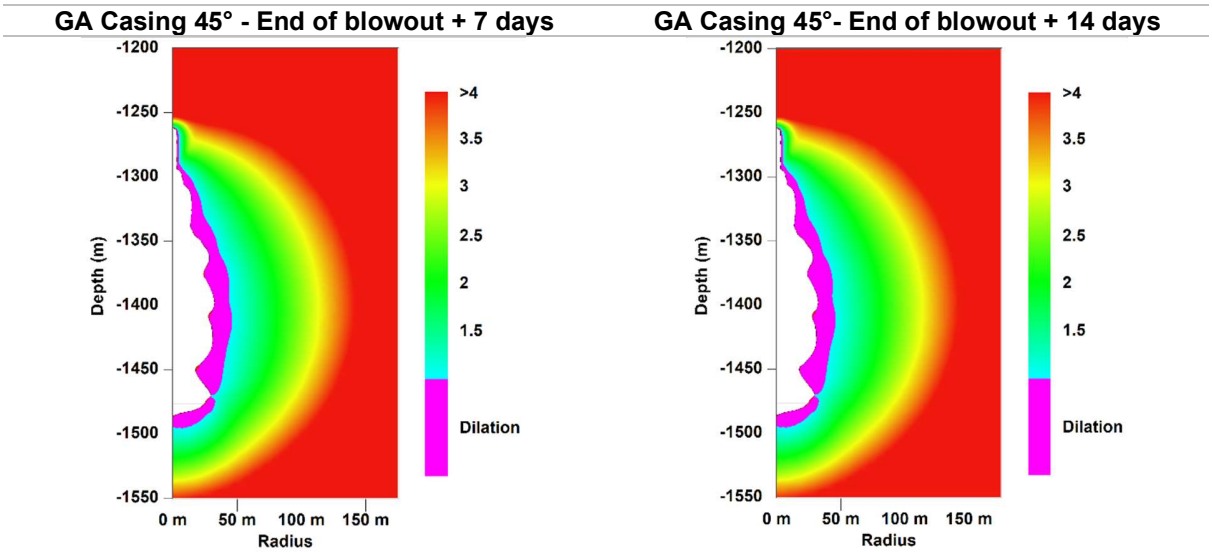

Figure 15. Factor of Safety (FoS) at 7 and 14 days after the blowout (GA, casing 45°C; cavern at atmospheric pressure (*14.7 psi*)).

3.3.3. Surrounding rock mass displacement

Radial displacement u_r is positive outward and negative inward (convergence). Vertical displacement u_z is positive upward (uplift) and negative downward (settlement). Figure 16 shows radial displacement. Inward motion is concentrated near the wall and decays rapidly with radius. The near-wall maximum grows slightly from 0.60 m (*1.97 ft*) at +7 days to 0.63 m (*2.07 ft*) at +14 days; beyond 100 m (*328 ft*), changes are negligible.

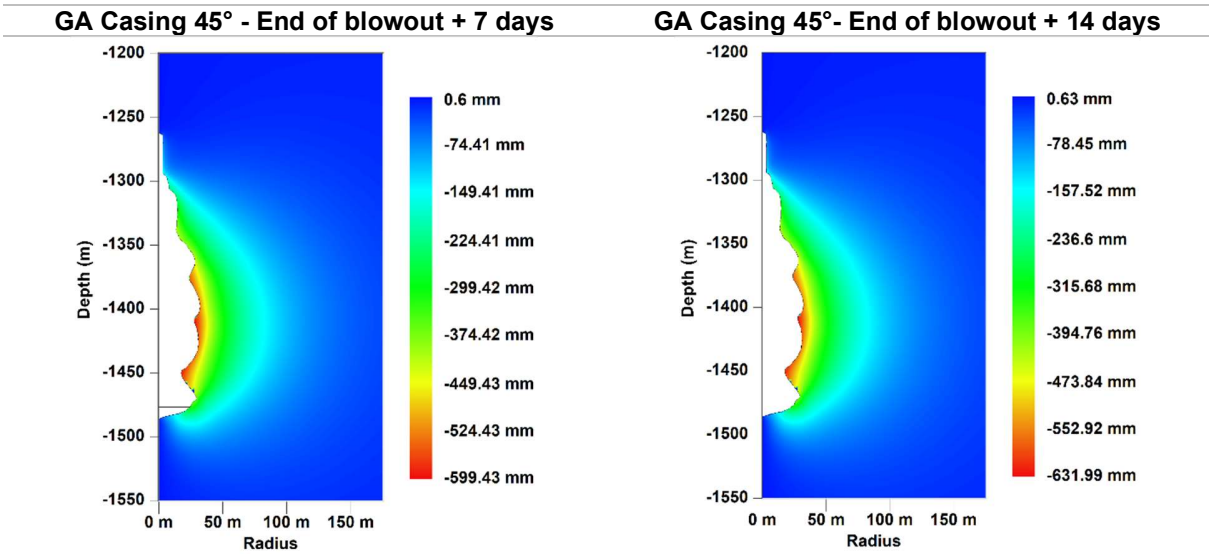

Figure 16. Radial displacement at 7 and 14 days after the blowout (GA, casing 45°C).

In the vertical displacement plot (Figure 17), the pattern is asymmetric, with uplift above the roof and subsidence near the floor. Peak magnitudes increase modestly from approximately +0.50 m (*1.64 ft*) to −0.21 m (*−0.69 ft*) at +7 days to approximately +0.53 m (*1.74 ft*) to −0.23 m (*−0.75 ft*) at +14 days. Both

radial and vertical motions are strongly localized around the cavern, consistent with the FoS maps and the observed decay of convergence rates during the second week.

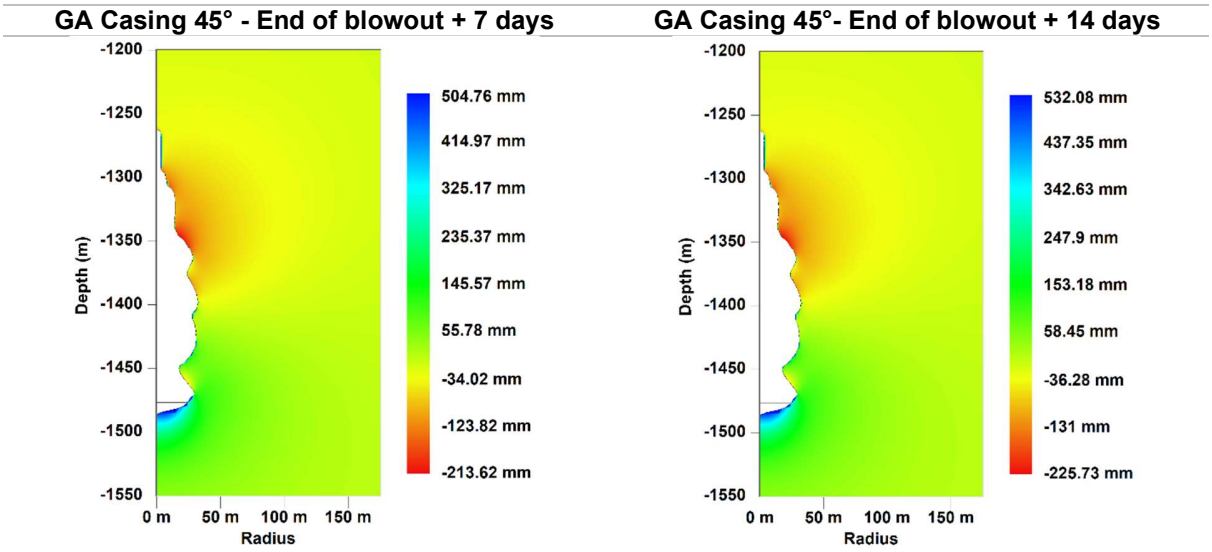

Figure 17. Vertical displacement at 7 and 14 days after the blowout (GA, casing 45°C; cavern at atmospheric pressure (*14.7 psi*)).

4. Discussion

The simulations fit the established causal chain: discharge → cooling → stress/strain → convergence; and align with prior semi-analytical and FE studies of gas-cavern blowdowns (Bérest et al., 2013; Djizanne et al., 2014, 2022a; Brouard Consulting & RESPEC, 2013; Brouard et al., 2022).

The GA/GB simulations successfully reproduce EZ53 discharge-cooling-mechanical sequence while scaling to larger systems. Using EZ53 as the baseline (volume 7,390 m³, initial pressure 15 MPa, blowout duration 3.65 hours), the significantly larger GA and GB caverns demonstrate proportional scaling across all parameters. Their volumes of 337,044 m³ (GA) and 288,125 m³ (GB), combined with higher initial pressures of 23-25 MPa, extend blowout durations to 102.48 hours (GA) and 94.80 hours (GB). Heat transfer scales proportionally from 11 MW in EZ53 to 34-35 MW in GA/GB, while initial mass flow increases from 36.4 kg/s to 90-92 kg/s. Importantly, cooling effects are severe but less extreme in the larger caverns: wellhead temperature minima improve from −63°C in EZ53 to approximately −52/-51°C in GA/GB, while the lowest cavern temperatures are substantially milder (−23°C in EZ53 versus −10°C in GA/GB). This scaling relationship confirms that event duration and heat exchange increase proportionally with inventory and hydraulic cross-section.

The discharge path emerges as the dominant control on persistence (casing short and intense; tubing longer and milder at the wall), while geometry/depth modulates magnitude; consistent with documented events and modeling envelopes. The near-field thermal response is confined to a thin layer along the cavern wall: temperatures reach their minimum early in the event and then recover by conduction, a timing that aligns with (and explains) the synchronized peak in convergence rate reported here and in prior THM studies.

Stability metrics align with the literature: Bérest effective stress transitions to near-tensile only in a narrow annulus, and $FoS \leq 1$ remains confined to the wall, while the far field remains stable (Bérest & Brouard, 2003; Djizanne et al., 2014). This localization, consistent across EZ53, GA, and GB caverns, aligns with salt damage mechanics that limit radial propagation during transient cooling (Habbani et al., 2025).

For surface risk, the longer tubing cases imply a longer dispersion window, whereas casing cases concentrate the thermal load at the wall; consistent with hydrogen-specific dispersion findings and calls for standard scenarios (Djizanne et al., 2022a; Portarapillo & Di Benedetto, 2021; Buzogany et al., 2023).

Assumptions here are conservative (99% H_2 at maximum service pressure) and axisymmetric; real GA/GB caverns are brine-filled. These choices bound behavior but justify reading results as upper limits. Adding 3-D geometry, bedding/heterogeneity, cohesive fracture, and tighter coupling to wellbore heat transfer and atmospheric dispersion would refine area thickness and consequence mapping.

5. Conclusion

A unified thermomechanical framework applied to two real caverns (GA, GB) shows that flow path governs blowout persistence and cooling footprint, while depth/geometry controls magnitudes of stress, FoS reduction, and convergence; initial gas temperature is secondary. Cooling creates a 5-10 m (*16.4 - 32.8 ft*) near-wall area, briefly lowering stability margins (effective-stress tension areas; $FoS \leq 1$) yet leaving the far field stable. Convergence is rapid at onset and then decays; most of the added loss occurs within the first week at atmospheric pressure (*14.7 psi*). These relationships align with incident syntheses and modeling studies and translate into practical guidance: prioritize flow-path management, monitor roof-proximal zones, plan for early post-event closure, and pair cavern assessment with well integrity checks. Embedding such blowout modeling in safety studies will support materials/operating-envelope choices and evidence-based emergency protocols for hydrogen storage in salt caverns.

6. Acknowledgements

This work received funding from the Clean Hydrogen Partnership of the European Union under grant agreements No. 101006751 (HyPSTER) and No. 101137892 (FrHyGe). The author thanks the HyPSTER consortium: Storengy; Armines-École Polytechnique; INOVYN; ESK; Element Energy; Ineris; Axelera; Brouard Consulting; Equinor; and the FrHyGe consortium: Storengy; Géostock; Artelys; Ineris; Capenergies Association; Armines-École des Mines de Paris; AXENS SA; IFP Energies Nouvelles; Enagás Transporte SA; ECO MED; ESK GmbH; GRTgaz; and Géométhane, for constructive discussions and support.

Disclaimer. The views and opinions expressed are those of the author only and do not necessarily reflect those of the European Union or the Clean Hydrogen Partnership; neither the EU nor the granting authority can be held responsible for them.

7. References

Arnold, C., Hanisch, P., & Pischner, M. (2010). *Long-term development and extension of the brine field and storage site Teutschenthal-Bad Lauchstädt in central Germany*. Proc. SMRI Fall Conference, Leipzig, 137-154.

Bérest, P. & Brouard, B. (2003). *Safety of Salt Caverns Used for Underground Storage*. Oil & Gas Science and Technology - Rev. IFP, 58(3), 361-384.

Bérest, P., Djizanne, H., Brouard, B. & Frangi, A. (2013). *A simplified solution for gas flow during a blowout in an H_2 or air storage cavern*. Proc. SMRI Spring Technical Conference, Lafayette, LA, 21-24 April.

Bérest, P., Karimi-Jafari, M. & Brouard, B. (2007). *Onset of tensile effective stresses in gas storage caverns*. Proc. SMRI Fall Meeting, 119-135. https://hal.science/hal-00560262

Brouard Consulting & RESPEC. (2013). *Analysis of Moss Bluff Cavern #1 blowout data*. SMRI Research Report 2013-01, 188 p.

Brouard, B. & Bérest, P. (2022). *Calibration of rock-salt thermal and mechanical parameters based on available field data*. Proc. SMRI Spring Meeting, Rapid City, SD.

Brouard, B., Zakharov, V., & Frangi, A. (2022). *Numerical modeling of the complex behavior of salt caverns*. International Geomechanics Symposium, Abu Dhabi. https://doi.org/10.56952/IGS-2022-028

Buzogany, R., Bernhardt, H., Réveillère, A., Fournier, C., Voegeli, S., & Duhan, J. (2023). *Hydrogen storage in salt caverns - Current status and potential future research topics*. SMRI Research Report 2023-1, 110 p.

DeVries, K. L., Mellegard, K. D., Callahan, G. D. and Goodman, W. M. (2005). *Cavern Roof Stability for Natural Gas Storage in Bedded Salt* (Report 850074), RSI-1829, prepared by RESPEC, Rapid City, SD, for the United States Department of Energy, National Energy Technology Laboratory, Pittsburgh, PA. https://doi.org/10.2172/850074.

Djizanne H. (2014). Mechanical stability of a salt cavern submitted to rapid pressure variations: Application to the underground storage of natural gas, compressed air, and hydrogen (in French). PhD dissertation, École Polytechnique, 274p. https://pastel.archives-ouvertes.fr/tel-01130986 (retrieved 5/05/2023).

Djizanne, H., Bérest, P., Brouard, B. & Frangi, A. (2014). *Blowout in gas storage caverns*. Oil & Gas Science and Technology - Revue d'IFP Energies nouvelles, 69, 1251-1267.

Djizanne, H., Brouard, B., Bérest, P. & Hévin, G. (2022). *Modélisation de l'éruption d'une cavité saline de stockage souterrain d'hydrogène*. 11èmes Journées Nationales de Géotechnique et de Géologie de l'Ingénieur, Lyon, 28-30 June.

Djizanne, H., Brouard, B., Bérest, P., Hévin, G. & Murillo Rueda, C. (2022). *Blowout from a hydrogen storage cavern*. Proc. SMRI Spring Technical Conference, Rapid City, SD, 4-5 May.

Habbani, H., Djizanne, H., Brouard, B. & Pouya, A. (2025). *Modeling dilatancy-induced damage in rock salt using DISROC: A joint-enriched finite element analysis for UHS*. SaltMech XI, Santa Fe, USA.

Halbgewachs, R., Coleman Hale, R., Seidlitz, H., Nieland, J., Seymour, P. & Mendes, S. (2023). Prud'homme Cavern No. 1: *Remediation & reactivation of a natural gas storage cavern*. Proc. SMRI Spring Technical Conference, Detroit, MI, 24-26 April.

Munson D. E. (1997). *Constitutive model of creep in rock salt applied to underground room closure.* International Journal of Rock Mechanics and Mining Sciences, Vol. 34 (2), pp. 233-247, https://doi.org/10.1016/S0148-9062(96)00047-2.

Munson D. E. and Dawson P. R. (1984), *Salt constitutive modeling using mechanism maps*. In H. Reginald Hardy, Jr & Michael Langer (eds.), Proc. 1st Conf. Mech. Beh. of Salt: 717-737. Clausthal-Zellerfeld: Trans Tech Pub.

Munson, D. E., 1998*. Analysis of Multistage and Other Creep Data for Domal Salts*, SAND98-2276, Sandia National Laboratories, Albuquerque, NM.

Munson, D. E., DeVries, K. L., Fossum, A. F., & Callahan, G. D. (1993). *Extension of the M-D model for treating stress drops in salt*, Proc. Mechanical Behavior of Salt III, Palaiseau, France. Ghoreychi, Bérest, Hardy et Langer (eds.), Trans Tech Pub, Clausthal-Zellerfeld, Germany, ISBN 0-87849-071-X, 31-44. DOI:10.2172/10173279.

Portarapillo, M. & Di Benedetto, A. (2021). *Risk Assessment of Large-Scale Hydrogen Storage in Salt Caverns*. Energies, 14(10).

Pouya, A. & Bemani, Y. P. (2015). *A damage-plasticity model for cohesive fractures. International Journal of Rock Mechanics and Mining Sciences*, 73, 194-202.

Réveillère, A., Bérest, P., Evans, D. J., Stower, M., Chabannes, C., Koopmans, T. & Bolt, R. (2017). *Past Salt Caverns Incidents Database: Part 1 - Leakage, Overfilling, and Blowout*. SMRI Research Report RR2017-2, 121 p.

Rittenhour, T. P. & Heath, S. (2012). Moss Bluff Cavern 1 blowout. Proc. SMRI Fall Technical Conference, Bremen, Germany, 30 Sept-3 Oct, 119-130.

Stolz, K. (2012). *Top kill on a natural gas storage cavern*. Proc. SMRI Spring Technical Conference, Regina, Saskatchewan, 23-24 April.

Thoms, R. L. & Martinez, J. D. (1980). *Blowouts in domal salt*. In Proceedings of the Fifth International Symposium on Salt (Vol. 1), Hamburg: Northern Ohio Geological Society, 405-411.

U.S. Department of Energy. (1980a). *OSC Strategic Petroleum Reserve West Hackberry Oil Storage Cavern Fire and Spill, After-Action Report I.*

U.S. Department of Energy. (1980b, February). *Strategic Petroleum Reserve West Hackberry oil storage cavern fire and spill of September 21, 1978*: *An environmental assessment*.

Zaim, M., Habbani, H., Djizanne, H., Brouard, B. & Pouya, A. (2025). *Stability analysis of a salt cavern subjected to a blowout scenario*. SaltMech XI, Santa Fe, USA.Arnold, C., Hanisch, P., & Pischner, M. (2010). *Long-term development and extension of the brine field and storage site Teutschenthal-Bad Lauchstädt in central Germany*. Proc. SMRI Fall Conference, Leipzig, 137-154.